Earth Planet. Sci. Lett. 644 (2024) 118925

Contents lists available at ScienceDirect

Earth and Planetary Science Letters

journal homepage: www.elsevier.com/locate/epsl

Changing shape of mantle heterogeneity by melt migration beneath mid-ocean ridges

Boda Liu [a,*], Yan Liang [b], Chuan-Zhou Liu [c,d]

[a] State Key Laboratory of Lithospheric and Environmental Coevolution, Institute of Geology and Geophysics, Chinese Academy of Sciences, Beijing, 100029, PR China
[b] Department of Earth, Environmental & Planetary Sciences, Brown University, Providence, RI, 02906, USA
[c] Laoshan Laboratory, Qingdao, 266237, PR China
[d] College of Earth and Planetary Science, University of Chinese Academy of Sciences, Beijing, 100049, PR China

ARTICLE INFO

Editor: Dr Fang-Zhen Teng

Keywords:
Mantle heterogeneity
Abyssal peridotite
Nd and Hf isotope ratios
Chromatography fractionation
Dispersion
Mid-ocean ridge

ABSTRACT

The common assumption that residual peridotites retain the Nd-Hf isotope ratios in the mantle source is debated because melt and solid of different isotopic compositions could undergo chemical exchange during melt migration, altering the isotopic signature of the source. By modeling the transport of chemical heterogeneities in the melting region beneath a mid-ocean ridge, we show that the shape of a chemical heterogeneity marked by Nd or Hf isotope ratio changes systematically through subvertical dispersion, stretching, compression, and shearing. The isotope ratios inside the chemical heterogeneity decay toward the values of background mantle. The amount of decay depends on the strength of dispersion, which itself is strongly dependent on the melt fraction in the melting region. When the maximum melt fraction is greater than 1%, buoyancy-driven melt flow relative to the solid causes subvertical dispersion of isotopic signals in the solid. Differential flows of the melt and solid also produce chromatography fractionation of Nd with respect to Hf, causing their isotope ratios to decouple. Compositions of the residue in Nd-Hf isotope ratio diagram do not record the endmembers in the source, instead they represent an area that covers part of the binary mixing line between the background mantle and the original heterogeneity. In the case of small melt fraction (<0.2%), the low permeability results in sluggish melt flow, weak dispersion, and negligible chromatography fractionation. Consequently, Nd and Hf isotope ratios in the residue remain coupled, representing the endmember isotope ratios in the source. The ridge model with larger melt fraction may correspond to the fast-spreading ridge, while the model with smaller melt fraction may correspond to the ultraslow-spreading ridge. The present study underscores the importance of melt migration processes beneath mid-ocean ridges on the deformation, mixing and decoupling of Nd-Hf isotope ratios in residual peridotites.

1. Introduction

The Earth's mantle is chemically heterogeneous across all scales, from the level of individual minerals to vast compositional domains. The formation of mantle heterogeneities are the results of billion years of mantle convection, plate recycling, etc. However, the size, shape, and distribution of mantle heterogeneities are difficult to constrain because most of the mantle is inaccessible. Available petrological records include mantle-derived magmas and peridotites. The former are mixtures of melts pooled from a sampling area that could be 100~200 km wide under mid-ocean ridges (The MELT Seismic Team, 1998), which would obscure the chemical signal of heterogeneities smaller than a few kilometers. Peridotites are more direct record. For example, abyssal peridotites, the residues of mantle melting beneath mid-ocean ridges, show more variable isotope ratios than mid-ocean ridge basalts (e.g., Snow et al., 1994; Stracke et al., 2011; Mallick et al., 2014). However, whether trace element and isotope ratio variations in these residual samples could represent the source or are results of mid-ocean ridge processes remains debated (e.g., Niu et al., 1997; Warren and Shimizu, 2010; Frisby et al., 2016). Therefore, understanding the effect of melting and melt migration processes beneath mid-ocean ridges on the preservation of chemical heterogeneities is essential to mantle geochemistry.

Models for the fractionation of trace elements during decompression melting of a heterogeneous mantle have been formulated for one-

* Corresponding author.
E-mail address: bodaliu@mail.iggcas.ac.cn (B. Liu).

https://doi.org/10.1016/j.epsl.2024.118925
Received 23 February 2024; Received in revised form 24 July 2024; Accepted 30 July 2024
Available online 20 August 2024

dimensional melting column or bundles of columns. In these models, chemical heterogeneities of prescribed size are represented by vertically stacked Gaussian, rectangular, or sinusoidal signals (DePaolo, 1996; Liang, 2008; 2020; Liu and Liang, 2017a, 2020; Bo et al., 2018). As the melt rises faster than the residual solid, the percolating melt would change the composition of the solid through chemical exchange. The resulting chemical heterogeneities recorded in the residue are stretched and dispersed (Navon and Stolper, 1987; Liu and Liang, 2017a; Bo et al., 2018; Liang and Liu, 2018). However, in more complicated but realistic models, melt and solid flow both vertically and horizontally and their

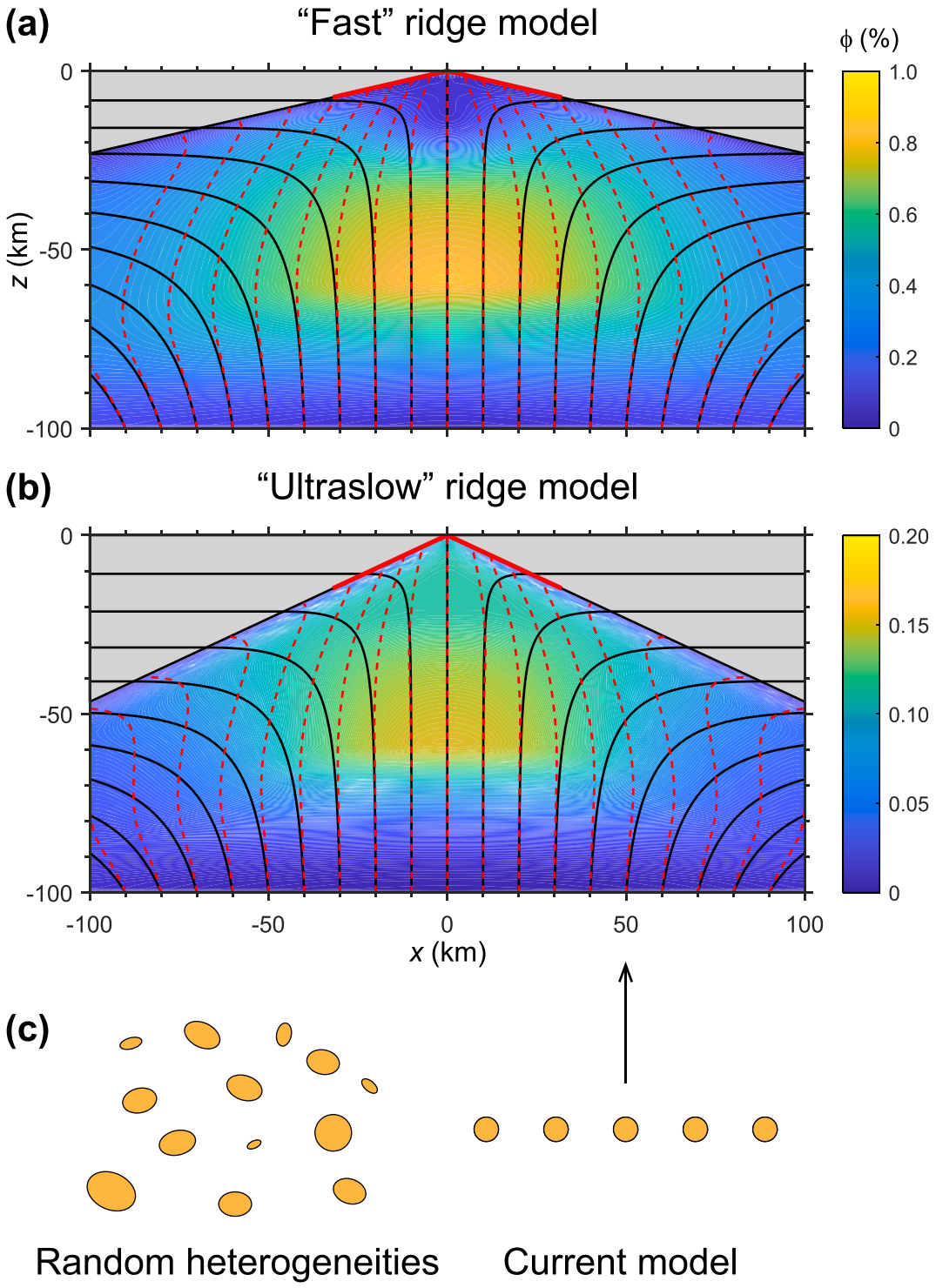

Fig. 1. Endmember models for mid-ocean ridges. The half-spreading rates for the model in (a) and (b) are 50 mm/yr and 7 mm/yr, respectively. We refer to these two endmember models as "fast" and "ultraslow" ridge model. The crustal thickness is 7.1 km in (a) and 1.4 km in (b) (not shown). Oceanic lithosphere has a wedge shape. Solid and dashed lines represent streamlines for the solid and melt, respectively. The pair of thickened red lines under the axis are decompaction channels that funnel the melt into the axis. (c) Schematic diagram illustrating the distribution of chemical heterogeneities in the source mantle. Left: random shape, size, and spacing. Right: the current model simulates chemical heterogeneities of a specific size one at a time by inputting circle shaped chemical heterogeneities at different lateral distances from the central axis ($x = 0$ km).

velocity fields diverge at shallow depth beneath the mid-ocean ridge (Morgan, 1987; Spiegelman and McKenzie, 1987; Braun et al. 2000; Katz and Weatherley, 2012; Baltzell et al., 2015). Moreover, the melting and melt migration processes are variable among ridges with different spreading rates (Parmentier and Morgan, 1990; The MELT Seismic Team, 1998; Bell et al., 2016; Saikia et al., 2021). More realistic melting models considering the production, migration, and distribution of melt would be warranted in studying the effect of melting processes on the composition and shape of chemical heterogeneities.

The purpose of this study is to demonstrate and quantify deformation and dispersion of chemical heterogeneities beneath mid-ocean ridges during decompression melting. We set up 2D ridge model that captures the first-order processes and features such as the production, distribution, and migration of melt beneath mid-ocean ridges (Fig. 1). We explore the dependence of residue composition on several factors including the melt fraction, the original size, and the type of chemical heterogeneities. The main results are that (1) chemical heterogeneities marked by Nd-Hf isotope ratios deform in a systematic pattern and (2) the melt fraction beneath mid-ocean ridges has a leading-order control on the dispersion and decoupling of Nd-Hf isotope ratios in the residue. The current study emphasizes the important effects of melting process on interpreting geochemical records in residual rocks.

2. Model

2.1. 2D ridge models for melting and melt migration

The degree of melting, melt distribution, and crustal thickness at mid-ocean ridges vary with spreading rate. Based on the minimum shear velocities beneath fast-spreading ridges, the maximum volume fraction of melt in the partially molten mantle or melt fraction is estimated to be 0.8% to 1.4% (The MELT Seismic Team, 1998; Harmon et al., 2009; Bell et al., 2016; Gao, 2016) (Fig. S1). The melt fraction beneath slow-spreading ridge is smaller, ranging from 0 to 0.6% based on geophysical interpretations (Wang et al., 2020; Saikia et al., 2021). For the 6–7 km thick oceanic crust at fast- and slow-spreading ridges, the maximum degree of melting is estimated to be 20% (Forsyth, 1993). At ultraslow-spreading ridge, the thin crust or absence of crust is the result of small degree of melting or no melting. Since the degree of melting plays a key role in affecting the melt fraction and crustal thickness, we set up two endmember ridge models with maximum degrees of melting of 22% and 4%, respectively. The maximum degree of melting could be due to a number of factors, such as the lid-effect, potential temperature, and solidus of the source mantle (e.g., Langmuir et al., 1977; Niu and Hékinian, 1997). Because upwelling rate is proportional to spreading rate, higher upwelling rate at fast-spreading ridge would produce stronger advective heat flux and thinner conduction lid than those at slow-spreading ridge. Consequently, decompression melting at fast-spreading ridge is expected to terminate at lower pressure, causing higher degree of melting compared to slow-spreading ridge given other factors the same (Niu and Hékinian, 1997). We consider a 200 km wide, 100 km deep mantle domain perpendicular to the ridge axis. The initial melting depth is 100 km. The final melting depth is 10 and 30 km in the model with half spreading rate of 50 mm/yr and 7 mm/yr, respectively.

Independent geochemical and petrological observations suggest that the majority (>70%) of the melt must be extracted into localized channels (Johnson et al., 1990; Johnson and Dick, 1992; Kelemen et al., 1997; Braun and Kelemen, 2002; Liang and Peng, 2010). Therefore, we also incorporate a channel network to model melt extraction. The distribution of melt channels can be constrained by field and laboratory observations (e.g., Kelemen et al., 1997; Holtzman et al., 2003), as well as results of geodynamic models specifically designed to model the formation of decompaction channels (Sparks and Parmentier, 1991; Hebert and Montési, 2010). As the mantle upwells, the channels start to form at 60 km depth or at locations of high shear strain as the mantle turns sideways (Liu and Liang, 2019). The melt produced in the residual matrix is extracted to the channel and flows subvertically until it encounters the lithosphere-asthenosphere boundary (LAB). The abrupt cooling and crystallization at LAB produce a permeability barrier, which in turn forces the residue beneath the LAB to decompact (Sparks and Parmentier, 1991; Spiegelman, 1993). The decompaction boundary layer beneath the sloped LAB then serves as channels that funnel the melt into the ridge axis. Liu and Liang (2019) used a prescribed steady-state channel network to explain melt distribution beneath mid-ocean ridge, the highly fractionated nature of LREE in residual abyssal peridotites, and U-series disequilibria in MORB. In this study we adapt their channel distribution in our 2D ridge model.

By modeling variable degrees of melting due to the lid-effect and melt extraction into a 2D-distributed channel network, our ridge models reproduce the crustal thickness and melt fraction at fast and ultraslow-spreading ridges (Fig. S1 in supplementary material). These two cases, depicted in Fig. 1, are by no means representative of realistic mid-ocean ridges in every detail. For simplification, we assume all components in the mantle have uniform melting rate. Therefore, the current model cannot examine the effect of heterogeneous melting rate on the transport of trace elements (e.g., Richter and Daly, 1989; Katz and Weatherley, 2012). With these caveats in mind, we refer to these two models as “fast” and “ultraslow” for convenience of description and discussion. In Section 4.5 we will discuss how heterogeneous melting rate and complex features of mid-ocean ridge would affect results produced by current models.

Our models also consider chemical disequilibrium induced by slow diffusion of Nd and Hf in pyroxene in the residue. Previous studies have examined the role of disequilibrium melting in determining the composition of residual peridotite (Navon and Stolper, 1987; Qin, 1992; Iwamori, 1993a,b; Van Orman et al., 2002; Liu and Liang, 2017a,b). In the present study, we aim to further advance our understanding by introducing 2D models for melting and melt migration beneath mid-ocean ridges.

2.2. Modeling chemical heterogeneity

The source mantle could consist of randomly distributed chemical heterogeneities of various sizes and shapes. The size, shape, and composition of a chemical heterogeneity change systematically during decompression melting. In this study, we quantify these changes by tracking individual heterogeneities in the melting region. Following the pseudo-2D model for melting a chemically heterogeneous mantle beneath mid-ocean ridges (Liu and Liang, 2020), we use time-dependent boundary conditions at the bottom of the model domain to describe the size and distribution of chemical heterogeneities marked by isotope ratios such as $^{143}Nd/^{144}Nd$ or $^{176}Hf/^{177}Hf$. We assume the shape of chemical heterogeneities is circular below the solidus with diameters ranging from 1 km to 10 km. This is in line with our recent work on the prevalent length scale responsible for Nd and Hf isotope variations in MORB and abyssal peridotites (Liu and Liang, 2017a). The isotopic composition of the background mantle is the depleted MORB mantle or DMM (Workman and Hart, 2005). We also assume that the chemical heterogeneity has either enriched EMII-like isotope ratios (Zindler and Hart, 1986; Jackson and Hart, 2006) or depleted isotope ratios (e.g., Stracke et al., 2011). The abundance of Nd and Hf in the isotopically enriched endmember (EMII) can be up to three times higher than that of DMM while the abundance of Nd and Hf in the isotopically depleted endmember (ultra-depleted mantle, UDM) can be up to 50% less than that of DMM. It is important to note that the production of enriched or depleted isotope ratios depends on the elemental concentration and other factors including the history of melt depletion and crust recycling (Stracke et al., 2003). Although endmember compositions (Table 1) used in current models are specific, our conclusions regarding the changing size and shape of chemical heterogeneities are not sensitive to specific choices of endmember compositions. We will begin with an EMII-like enriched endmember for heterogeneities in Section 3 and generalize

Table 1
Compositions of geochemical endmembers and partition coefficients used in the model.

	EMII	UDM	DMM*	Partition coefficient†	
	Abundance (ppm)			k_0	k_p
Nd	0.483 to 1.45	0.241 to 0.483	0.483	0.0247	0.1193
Hf	0.127 to 0.381	0.0635 to 0.127	0.127	0.0304	0.1134
	Isotope ratios				
$^{143}Nd/^{144}Nd$	0.5124	0.5136	0.5133		
$^{176}Hf/^{177}Hf$	0.2828	0.2836	0.2835		

* DMM is the depleted-DMM from Workman and Hart (2005).
† The bulk partition coefficient is calculated as $k = (k_0 - F^*k_p)/(1\text{-}F)$. F is the degree of melting. Bulk solid–melt partition coefficient at the onset of melting, k_0 and bulk solid–melt partition coefficient, k_p for the melting reaction are average values for melting along the 1300 °C mantle adiabat for the DMM starting composition (Sun and Liang, 2012, 2014; Yao et al., 2012; Liang and Liu, 2016).

these results through an empirical model for arbitrary isotopic and elemental compositions of endmembers in Section 4.1.

The governing equations for the conservation of trace elements have been originally derived in the framework of two-phase flow (McKenzie, 1984; Richter, 1986), and later adapted by several studies (Iwamori, 1993a; Lundstrom, 2000; Jull et al., 2002; Liang, 2003) to incorporate disequilibrium melting and melt transport in chemically isolated channels. The set of equations and the numerical methods are the same as a previous pseudo-2D study except for the inclusion of 2D flows of the melt and solid (Liu and Liang, 2020) (supplementary material). We focus on Nd isotope ratio in the residue because it is more resilient to hydrothermal alteration than Sr and has better data coverage than Hf (Mallick et al., 2015; Warren, 2016). Results of Hf isotope ratio will be compared to available data in Section 4.3. To model an isotope ratio, we calculate the concentration of the two nuclides (e.g., ^{143}Nd and ^{144}Nd) independently before taking their ratio. The relative error for the concentration of Nd and Hf is 10^{-9}, which ensures accuracy at the 7th decimals in $^{143}Nd/^{144}Nd$ or $^{176}Hf/^{177}Hf$ or 2nd digit after decimals in ε_{Nd} and ε_{Hf}. The spatial resolution of our numerical models is 300 m which is sufficient for modeling kilometer size chemical heterogeneities in this study.

3. Results

3.1. Deformation and dispersion beneath the "fast" spreading ridge

We first present the patterns of deformed chemical heterogeneities based on the "fast" ridge model (Fig. 2a and b). The trajectory of chemical heterogeneity follows the flow of the mantle in the lower part of the melting domain where the flow fields of the melt and solid are subvertical but is displaced above the streamline of the solid when the mantle flow turns sideways. If the interstitial melt were in chemical equilibrium with the residual solid, the effective transport velocity of the isotopic signal would be a weighted average of the velocity of the solid and that of the percolating melt (McKenzie, 1984; Navon and Stolper, 1987). The velocity of the interstitial melt relative to the solid is subvertical as it is driven mostly by buoyancy of the melt. The trajectory of chemical heterogeneities is therefore offset above the streamline of the mantle (Fig. 3b). Due to the slow lattice diffusion of Nd in the residual solid, chemical exchange of Nd between the solid and the melt is not fast enough to attain local equilibrium. Consequently, the melt from the heterogeneity disperses the chemical and isotopic signal toward the direction of melt flow (Fig. 3). The dispersion causes the isotopic signal in the melt to mix with that in the background mantle. The peak ε_{Nd} inside the heterogeneity, i.e. the isotope ratio most similar to the endmember, decays from the value of the original heterogeneity toward the value of background DMM mantle.

To quantify the deformation pattern, we draw outlines of deformed chemical heterogeneities and use image analysis to extract the long axis and short axis of each elliptical shaped heterogeneity (Figs. 3a and b and 4a). The extent of deformation depends on the location where the heterogeneity enters the bottom of the melting column. Heterogeneity below the ridge axis is stretched and dispersed vertically from 100 km depth to 40 km depth as melting produces higher porosity (Fig. 1a) and acceleration of the melt, thus faster effective transport velocity. The stretched shape reaches a maximum length of 13 km or 17 km at 40 km depth for original diameter 5 km or 10 km, respectively (Fig. 4a).

The upwelling of chemical heterogeneity decelerates above 40 km depth (Fig. 4a). The porosity decreases (Fig. 1a) and the melt velocity slows down to match the reduced upwelling rate of the mantle. Consequently, the effective transport velocity for the case of chemical equilibrium also decelerates. The dispersed heterogeneity is vertically compressed beneath the ridge axis. This vertical compression is opposite to the case of constant melting rate where the upward melt velocity increases all the way to the top of the melting column (Liang and Liu, 2018). At 20 km depth, the length of the heterogeneity is compressed to 9–11 km. As the heterogeneity further rises and reaches the ridge axis, it would be split into two parts which then move away from the axis with the oceanic lithosphere (Fig. 2a and b).

Following a chemical heterogeneity entering the melting region at 30 km away from the central axis, it is first sheared by the mantle flow and forms an oblate ellipse (labeled A2 in Fig. 3a). The elliptical shaped heterogeneity rises and rotates with the flow of the mantle. Increased melt flux then creates a subvertical dispersion tail superimposed on the oblate-shaped heterogeneities (A3 in Fig. 3a). When the heterogeneity is at 40 km depth, the length of the dispersed signal reaches a maximum of 11 km or 17 km for an original diameter 5 km or 10 km, respectively (A4 in Fig. 3a). Deformation continues as the mantle flow turns sideways above 30 km depth. The chemical heterogeneity (A5-A7 in Fig. 3a) is in between the hypothetical heterogeneity traveling at the velocity of the solid (C5-C7 in Fig. 3c) and that traveling at the effective transport velocity of the melt (B5-B7 in Fig. 3b). The final elliptical shaped heterogeneity would be preserved in the oceanic lithosphere (A8 in Fig. 3a).

3.2. Deformation and lack of dispersion beneath the "ultraslow" spreading ridge

The deformation of chemical heterogeneities in the "ultraslow" ridge model is controlled by the flow of the mantle (Fig. 2c and d). Because of the much smaller porosity compared to the case presented in the previous section, the rate of porous flow is slower. The effective transport velocity is close to the velocity of the mantle. The transport of chemical signals follows the streamline of the solid.

Heterogeneity below the ridge axis rises with the upwelling mantle and is undeformed until it is 10 km within the ridge axis. Then it splits into two parts and moves away from the axis. The corner flow of the mantle shears chemical heterogeneities entering the melting region at some distance away from the central axis. The original circle is sheared into oblate ellipse with long axis up to double the original diameter (Fig. 4b). As the strain is controlled by the mantle flow, the shape as characterized by the aspect ratio is independent of the size of the heterogeneity (Fig. 4b). The isotope ratio of incompatible element enriched heterogeneity is preserved in the residue of the ridge with small melt fraction (Fig. 4b). In the absence of dispersion, one can in theory map the spatial distribution of Nd isotope ratios in the residue and reconstruct the exact shape of chemical heterogeneities in the source by reversing the shear deformation using the corner flow model.

To summarize, the deformation pattern of chemical heterogeneities depends on the physical process of melt migration and mantle flow. The observed melt fraction (~1%) beneath fast-spreading ridge would produce strong vertical dispersion of chemical heterogeneity. The dispersion also causes the isotope ratio of heterogeneity to mix with the surrounding mantle. Porosity beneath slow and ultraslow-spreading

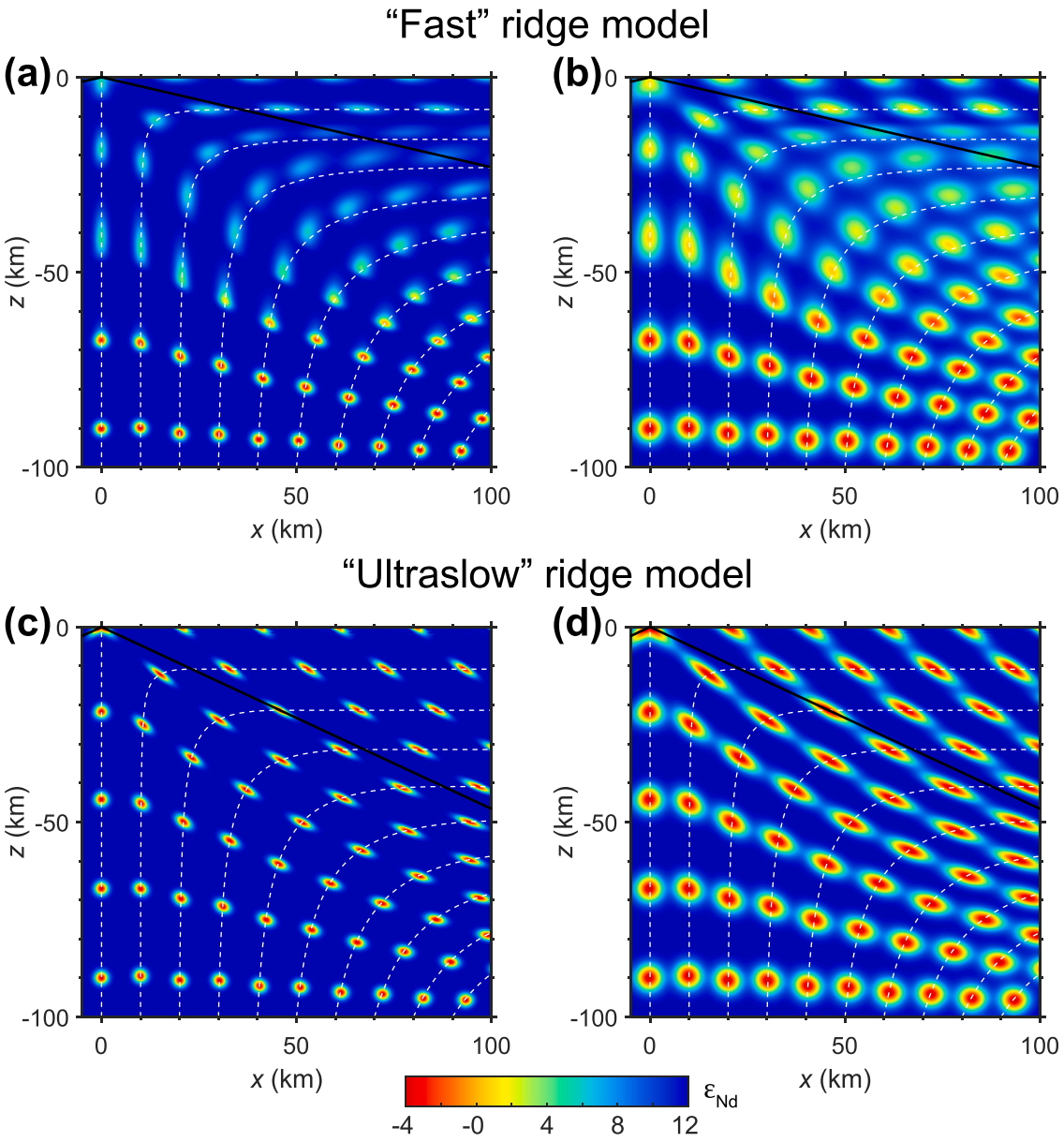

Fig. 2. The deformation and dispersion of chemical heterogeneities beneath the "fast" ridge model (a, b) and the "ultraslow" ridge model (c, d). Trains of circle shaped heterogeneities, originally 5 km (a, c) and 10 km diameter (b, d), enter the bottom of the melting region and undergo stretching, shearing, and dispersion along transport. White dashed lines represent streamlines for the solid. The time interval between two consecutive heterogeneities is 0.1 or 0.7 Myr for fast and ultraslow ridges. The color scale is for the value of ε_{Nd} ranging from EMII to the background DMM.

centers is controversial. If the asthenosphere beneath these ridges had smaller melt fraction (<0.2%), the magnitude of dispersion would be negligeable, and the deformed shape of chemical heterogeneity would be the result of shear due to mantle flow.

4. Discussion

4.1. Size and composition of chemical heterogeneity

In general, the ability of chemical heterogeneity to preserve the endmember isotope ratio increases with the elemental abundance in the original heterogeneity. Fig. 5 demonstrates the Nd isotopic heterogeneity in the residual solid using different elemental abundances (0.29 to 1.7 ppm) or isotope ratios for the heterogeneities in the source. Because isotopically enriched EMII heterogeneities tend to have higher abundance of Nd than isotopically depleted UDM heterogeneities, the enriched isotope ratios of EMII are better preserved than the depleted isotope ratios of UDM. When there is less abundance of Nd in the original heterogeneity, the decay of isotope ratio in the residue is stronger. The size of the heterogeneity ends up smaller than the case of higher original abundance, whereas their overall shape remains the same. Simulations of Hf isotopic heterogeneities also demonstrate stronger decay of endmember isotope ratios for lower abundances of Hf in the endmember (Fig. S2 in supplementary material).

In the following, we conduct a series of simulations using different sizes for heterogeneity of EMII and UDM isotope ratios, respectively. To quantify the preservation of isotope ratio in the residue, we focus on the peak isotope ratio (the most enriched or depleted for EMII or UDM endmember) in the heterogeneity after mid-ocean ridge processes. As demonstrated by earlier results, the effect of dispersion is accumulative and depends on the trajectory of the residual solid. To isolate the effect of size and composition of chemical heterogeneity, we select a specific

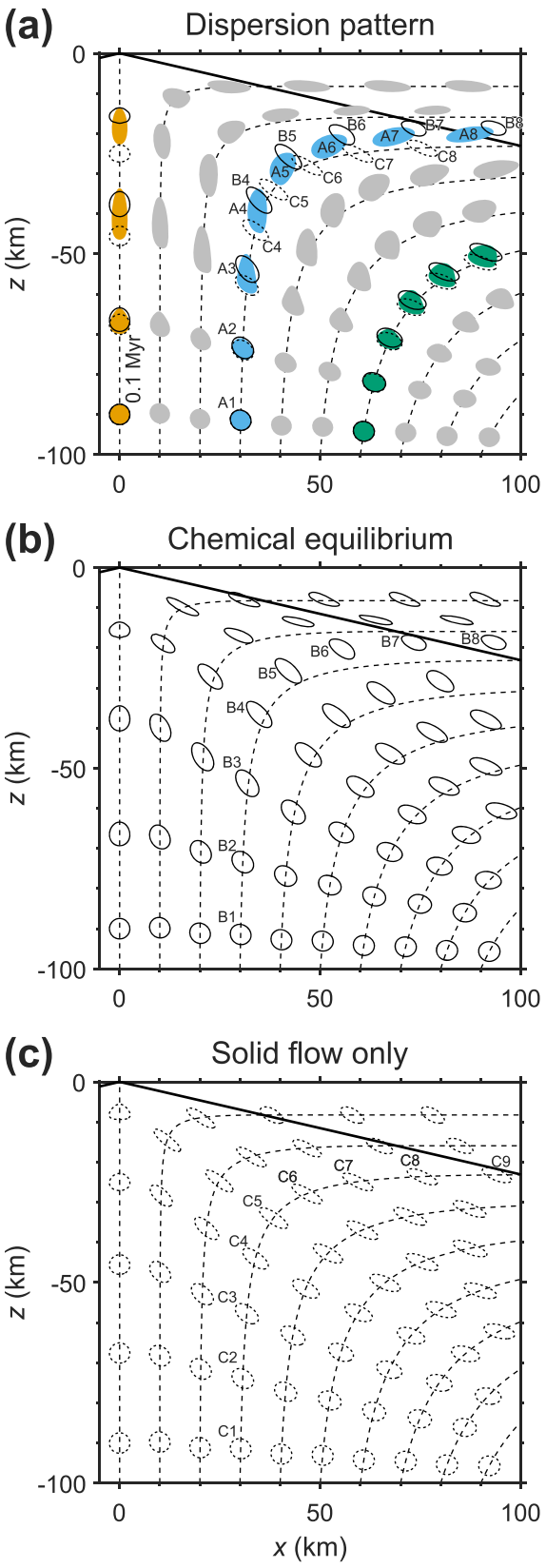

(caption on next column)

Fig. 3. Comparing the shape of chemical heterogeneities (a) to imagined patterns produced by equilibrium transport (b) and solid flow (c) beneath the "fast" ridge model. Filled shapes in panel (a) represent chemical heterogeneities marked by ε_{Nd}. The value corresponding to the outline is tenth quantile between the isotope ratio of DMM and that of EMII. The original shape is 5 km-diameter circle (the same as Fig. 2a). Dashed lines are streamlines of the mantle. Solid outlines in panel (b) are the shape of chemical heterogeneities assuming percolating melt is in chemical equilibrium with the solid. Dotted outlines in panel (c) are the shape of chemical heterogeneities if there is no melting. Superimposed on one train of heterogeneities in panel (a) are shapes in panels (b) and (c).

trajectory, which starts at 10 km away from the central axis and ends up in the wedge-shape lithosphere at ~8 km depth (Fig. 2).

Fig. 6 summarizes results of peak isotope ratios from our numerical simulations. The abundance of Nd in heterogeneities of EMII isotope ratio can be variably enriched relative to DMM. Simulations assuming heterogeneities of EMII isotope ratio has the same Nd abundance as DMM provide upper bounds for the amount of lost isotopic variability. For example, a 7 km-diameter heterogeneity with EMII isotope ratio would lose at most 50% contrast of its isotope ratio with respect to DMM for the "fast" ridge model. Similarly, assuming a heterogeneity of UDM isotope ratio has the same Nd abundance as DMM provides lower bounds for the amount of lost isotopic variability. If a heterogeneity in the source has UDM isotope ratio and 7 km diameter, it would lose at least 50% contrast of its isotope ratio with respect to DMM at the "fast" ridge model. Current results also suggest that residues at slow and ultraslow ridges could record larger variation in Nd isotope ratios compared to residues at fast ridges for the same size and composition of geochemical endmember.

The systematic variations of the peak isotope ratio in the shallow residual mantle observed in our numerical simulations can be quantified by an empirical model similar to that of Liu and Liang (2020) for mixing of pooled melts from a 2D melting region:

$$\frac{X}{Y}=\frac{(1-f)\cdot\left(\frac{X}{Y}\right)_D+f\cdot\left(\frac{X}{Y}\right)_E\cdot\frac{C_E}{C_D}}{(1-f)+f\cdot\frac{C_E}{C_D}}, \tag{1}$$

where $\frac{X}{Y}$ is the isotope ratio, such as $\frac{^{143}Nd}{^{144}Nd}$ or $\frac{^{176}Hf}{^{177}Hf}$, subscripts D and E represent the background depleted mantle and the geochemical endmember of the heterogeneity; C_D and C_E are the concentrations of the trace element, such as Nd or Hf, in the depleted mantle and the original heterogeneity, respectively; f, a function of the size of the chemical heterogeneity, is a weighing factor that varies between 0 and 1. For the 2D ridge model considered in this study, we found that the weighing factor f can be approximated by the error function (*erf*):

$$f=erf\left(\frac{L}{L_D}\right), \tag{2}$$

where L is the diameter of the original heterogeneity; L_D is a dispersion length scale specific to the ridge model. The magnitude of dispersion is strongly controlled by the presence of melt. Larger porosity would cause faster melt flow, stronger dispersion, and larger dispersion length scale (supplementary material). Because the magnitude of dispersion is not uniformly distributed, the value of L_D cannot be calculated from a simple scaling relationship. Below, we will estimate L_D empirically.

Eq. (1) is a generalization of the classic mixing model of Langmuir et al. (1978). It differs from the mixing equation for pooled melt (Liu and Liang, 2020) in the choice of the weighing function f. By fitting peak isotope ratios in numerical results (solid lines in Fig. 6), we find that the value of L_D for Nd is 14.5 km for the "fast" ridge model and 2.2 km for the "ultraslow" ridge model. We have also run numerical simulations for Hf isotope ratios and found that the value of L_D for Hf is 13.4 km and 2.3 km for "fast" and "ultraslow" ridge model, respectively (Fig. S5 in

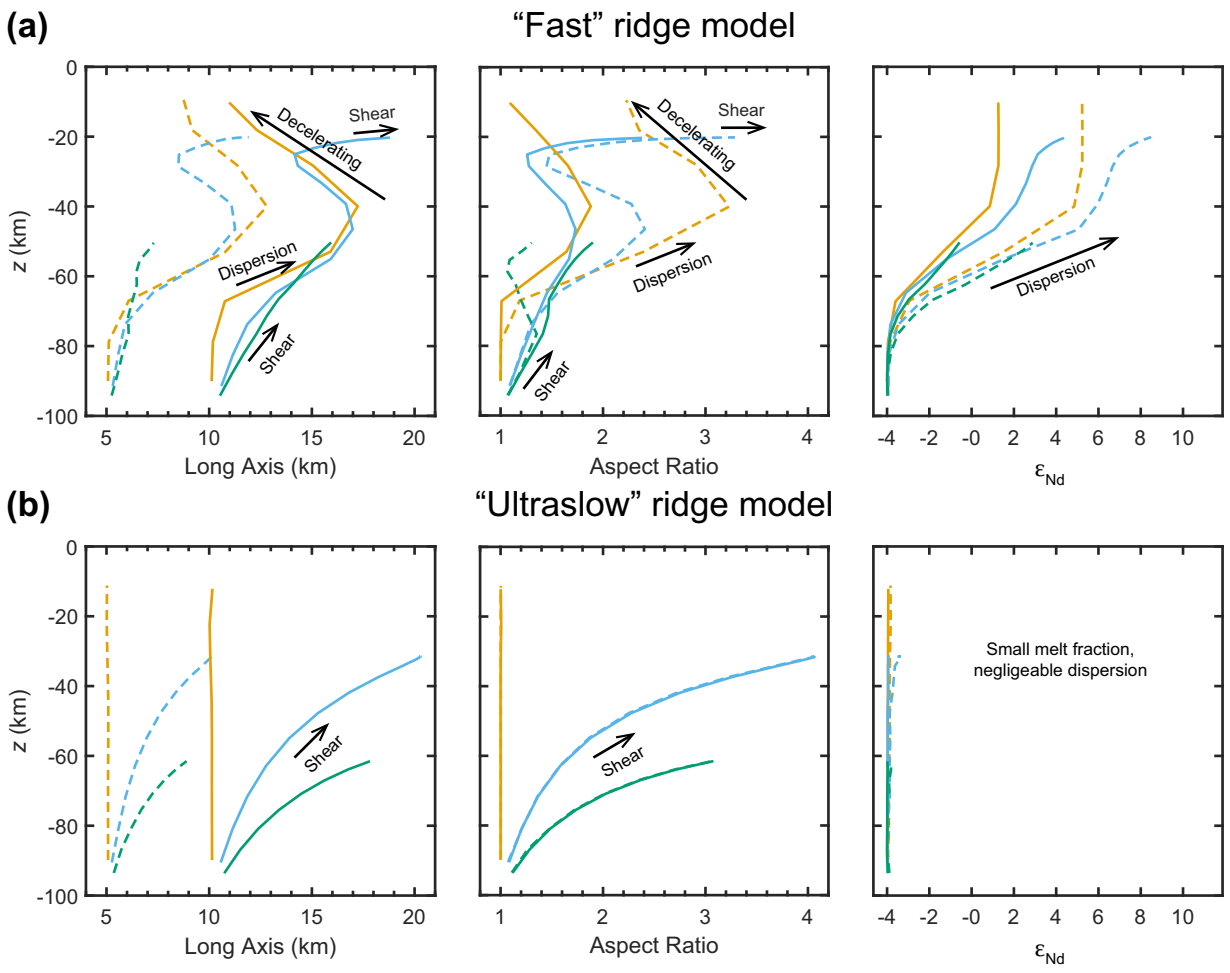

Fig. 4. The along-transport variation of the long axis, aspect ratio (long/short), and peak ε_{Nd} of the chemical heterogeneities beneath the "fast" ridge model (a) and the "ultraslow" ridge model (b). The color of the line corresponds to the three trains of heterogeneities entering the melting region at $x = 0$ (orange), 30 km (blue), and 60 km (green). Their trajectories are highlighted with the same color in Fig. 3a. Dashed and solid lines are for original diameter of 5 km and 10 km, respectively.

supplementary material). According to Eqs. (1) and (2), if the Nd (or Hf) abundance in the endmember is the same as DMM, Nd (or Hf) isotope ratio in the endmember would be preserved when the size of heterogeneity is larger than L_D, i.e., 2~15 km. This is consistent with the conclusion of Liu and Liang (2017a) based on simplified 2D models.

4.2. Implications for observed Nd isotope ratios in residual peridotites

Observations on the Nd isotope ratios of asthenospheric mantle are mostly from abyssal peridotites sampled at slow and ultraslow-spreading ridges (Snow et al., 1994; Salters and Dick, 2002; Cipriani et al., 2004; Warren et al., 2009; Stracke et al., 2011; Mallick et al., 2014, 2015; Sani et al., 2023). There are fewer Nd isotope data of peridotites from present-day fast-spreading ridge (Wendt et al., 1999). To complement these abyssal peridotites, six peridotites from Oman ophiolite (McCulloch et al., 1981; Yoshikawa et al., 2015) with estimated paleo half-spreading rate of 50–100 mm/yr (Rioux et al., 2012) are included in this study. Available data suggests that residues at fast spreading ridge record a smaller range of Nd isotope ratio compared to those at slow and ultraslow ridges (Fig. 6), which coincides with the prediction of stronger dispersion and mixing in the "fast" ridge model compared to "ultraslow" ridge model assuming the same size and elemental abundance of heterogeneities beneath different ridges. Therefore, the observed difference in the range of residual compositions may be attributed to the interplay of different melt migration processes and diverse sources for various ridge segments (Sanfilippo et al., 2019).

Results shown in Fig. 6 suggest small-scale variations (10–100 m) are homogenized during melting and melt migration under fast-spreading ridges. Some abyssal peridotites and massif peridotites exhibit small-scale chemical variations as a result of exceptionally low porosity in the melting region or recent metasomatism (e.g., Bodinier 1990; Warren and Shimizu, 2010). If these peridotites get recycled into the mantle and enter a melting region beneath mid-ocean ridge, their small-scale chemical variations are expected to smooth out if melt percolation is pervasive. Although a single small-scale heterogeneity is homogenized, a cluster of small-scale heterogeneities may still preserve partially the geochemical signature and represent a weaker and broader signal in the residue.

4.3. Can melting and melt migration processes produce decoupled Nd-Hf isotope ratios in residual peridotites?

Decoupled Nd-Hf isotope ratios in peridotites, defined as those compositions above or below the mantle array in Nd-Hf diagram, is an important observation in mantle geochemistry. In general, the depleted or enriched isotope ratios must be the result of long-term growth followed by more recent metasomatism (e.g., Salters and Zindler, 1995; Bizimis et al., 2004; Stracke et al., 2011). However, decoupled Nd-Hf isotope ratios could be the result of recent processes such as sea water alteration, chromatography fractionation, element-dependent dispersion, and melt-rock interaction (e.g., Salters and Hart, 1991; Stracke et al., 2011; Tilhac et al., 2022). Building on our 2D numerical model,

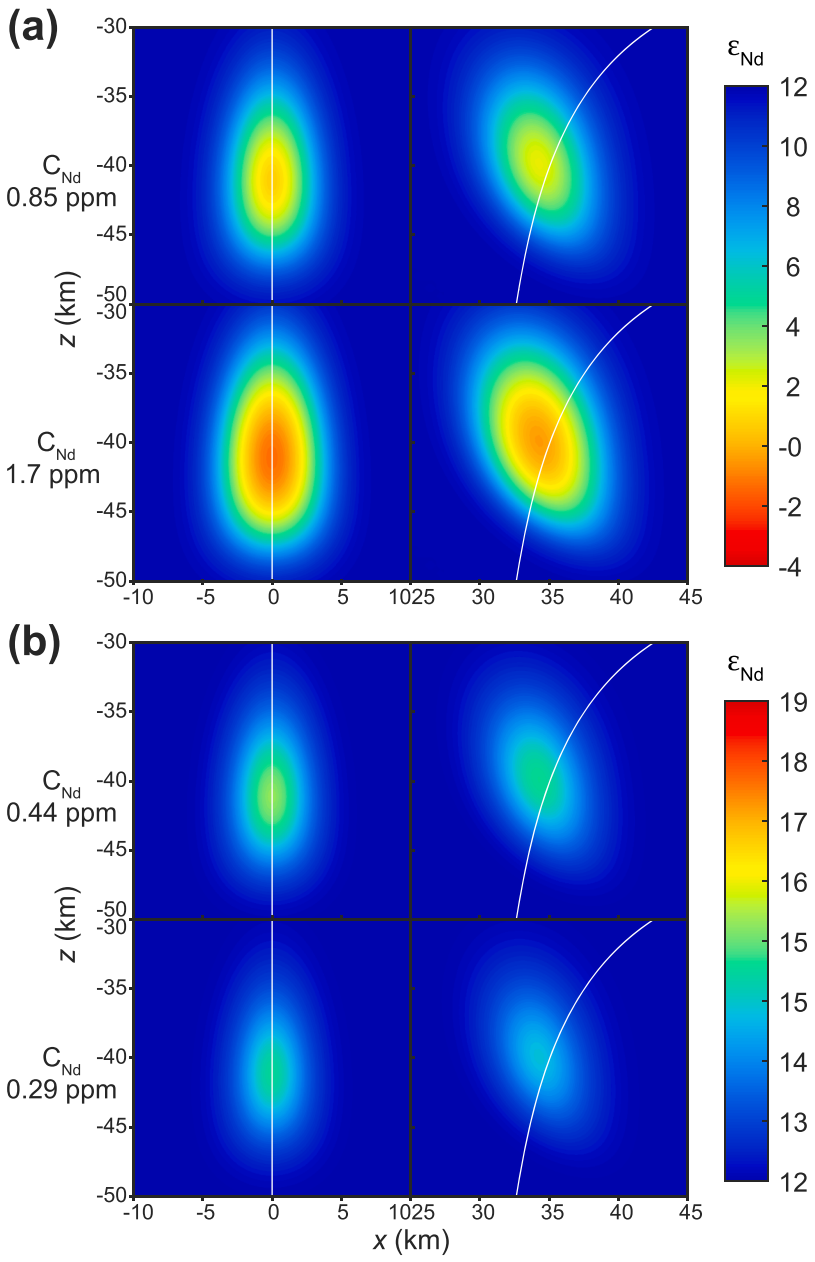

Fig. 5. Dispersion of chemical heterogeneities with different endmember compositions beneath the "fast" ridge model. The Nd isotope ratio of the original chemical heterogeneity is EMII (a) or ultra-depleted mantle (UDM) (b). The abundance of Nd in these endmembers ranges from 0.29 to 1.7 ppm. For reference, the abundance of Nd in DMM is 0.58 ppm (Workman and Hart, 2005). White lines represent streamlines for the solid. The diameter of original heterogeneity is 10 km. We assume the chemical heterogeneities have the same major element composition and melting rate as depleted mantle. Shown here are representative chemical heterogeneities at 40 km depth right beneath the ridge or 35 km away from the central axis.

here we explore the potential effects of chromatography fractionation and dispersion on the decoupling of Nd-Hf isotope ratios in residual peridotites.

At the location of maximum melt fraction in the "fast" ridge model, the effective vertical transport velocity of Nd is 5% faster than Hf (Table S2 in supplementary material). Such small difference is sufficient to cause chromatography fractionation, i.e., a chemical heterogeneity defined by Nd isotope ratio is advected ahead of that defined by Hf isotope ratio (Fig. 7a). Due to different effective transport velocities of Nd and Hf, the displacement of Nd signal relative to Hf signal gradually increases along the trajectory. If a 5 km-diameter heterogeneity rises straight up to the ridge axis (at $x = 0$), 62% area of the Nd signal ends up overlapping with the Hf signal. If a heterogeneity of the same size and original composition enters the melting region 20 km away from the central axis, only 15% area of the Nd signal overlaps with the Hf signal. The extent of displacement/overlap also depends on the original size of the heterogeneity. A smaller heterogeneity marked by Nd could be completely separated from that of Hf (Fig. S6 in supplementary material).

Spatially separated signals of Nd and Hf in residues produce decoupled isotope ratios in Nd-Hf isotopic space. Assuming the mantle source contains both enriched and depleted chemical heterogeneities, the composition of the residue observed in "fast" ridge model forms a pair of wings in the Nd-Hf isotopic space (Fig. 8a). If the chemical heterogeneity is EMII, the part of Nd signal ahead or after that of Hf produces compositions above or below the mixing line between EMII and DMM. The overlapping area of Nd and Hf signal produces compositions with enriched Nd and Hf isotopic signals. These compositions also form an

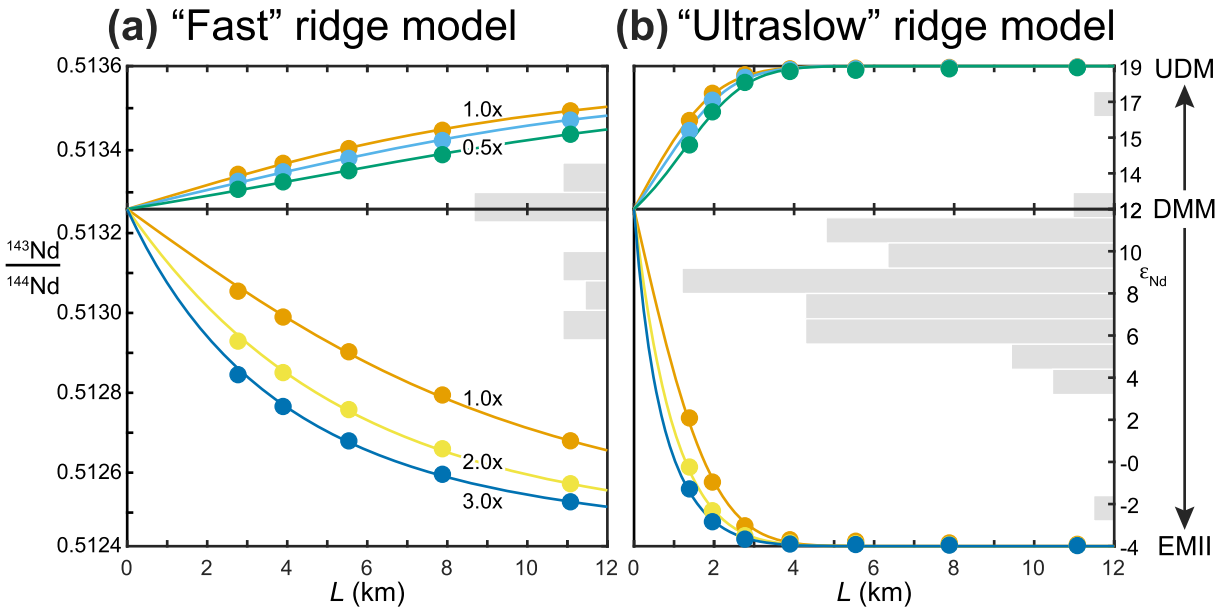

Fig. 6. The range of Nd isotope ratio in the residue beneath the "fast" ridge model (a) and the "ultraslow" ridge model (b). The range at given size is defined as the interval between the peak isotope ratio in the simulation using originally EMII endmember and that using UDM endmembers. The abundance of Nd in the source heterogeneity in EMII and UDM endmember is variably enriched (1, 2, 3 times) or depleted (1, 0.75, 0.5 time) relative to DMM. Solid lines are calculated using Eqs. (1-2) with $L_D = 14.5$ km (a) or 2.2 km (b). Histograms are Nd isotope ratios in samples from a paleo fast-spreading ridge (Oman, $N = 6$), present-day fast-spreading ridge (EPR, $N = 7$), and present-day ultraslow ridges (Gakkel, SWIR, etc. $N = 88$). Data are from the literature (McCulloch et al., 1981; Snow et al., 1994; Wendt et al., 1999; Salters and Dick, 2002; Cipriani et al., 2004; Warren et al., 2009; Stracke et al., 2011; Mallick et al., 2014, 2015; Yoshikawa et al., 2015; Sani et al., 2023). One sample with extreme $^{143}Nd/^{144}Nd$ of 0.5137 from Gakkel ridge (Stracke et al., 2011) is outside of the plotted range.

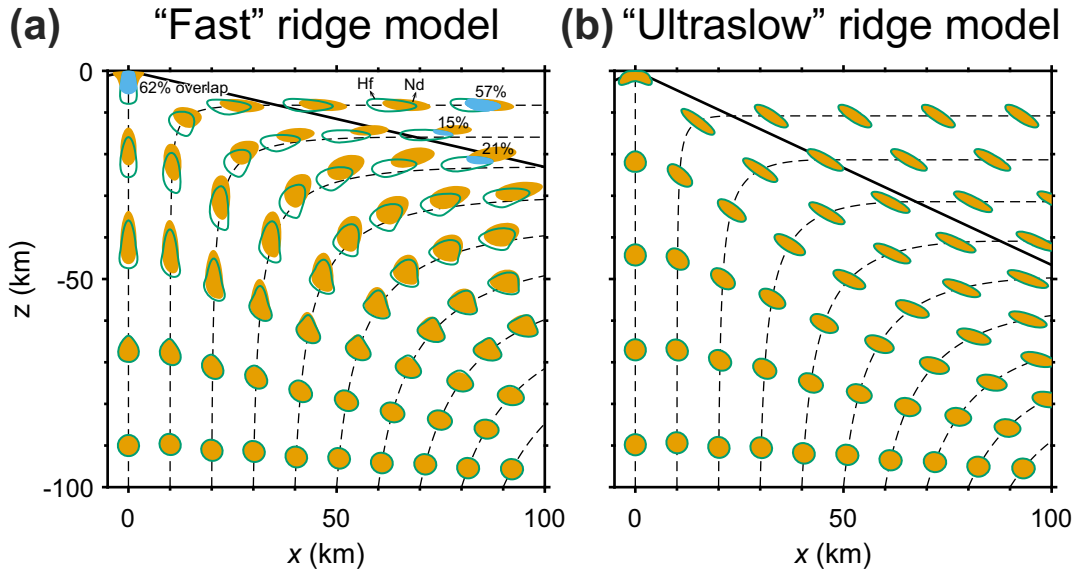

Fig. 7. Displacement and decoupling of chemical heterogeneities marked by Nd (yellow filled) and Hf (green outlines) isotope ratios beneath the "fast" ridge model (a) and the "ultraslow" ridge model (b). In the "fast" ridge model, Nd isotopic signal is physically displaced downwind relative to the Hf isotopic signal that is derived from the same original heterogeneity. Overlapping areas of Nd-Hf isotopic signals at four trajectories are highlighted in blue. In the "ultraslow" ridge model, Nd and Hf isotopic signals stay coupled.

area which only covers one-third of the mixing line between EMII and DMM if the original diameter is 5 km (Fig. 8a). Using the same size but UDM composition for the original heterogeneity, the compositional wing on the depleted side only covers 1/10 of the mixing line between UDM and DMM. These results are consistent with previous findings that lower abundance of Nd (or Hf) results in stronger decay of endmember isotopic ratios (c.f. Fig. 5). We found that the size of the compositional wings increases with the size of the original heterogeneity (Fig. S7 in supplementary material).

With smaller melt fraction in the "ultraslow" ridge model, the effective transport velocity of Nd is at most 0.2–0.3% faster than that of Hf (Table S2 in supplementary material). Consequently, Nd and Hf isotopic signals observed in our simulations stay coupled in both physical (Fig. 7b) and Nd-Hf isotopic space (Fig. 8b). Paired Nd and Hf isotopic ratios are available for abyssal peridotites sampled at ultraslow ridges (Stracke et al., 2011; Mallick et al., 2014, 2015; Sani et al., 2023). All samples ($N = 34$) except for five form a trend subparallel to the mantle array passing through the compositional field of MORB and OIB

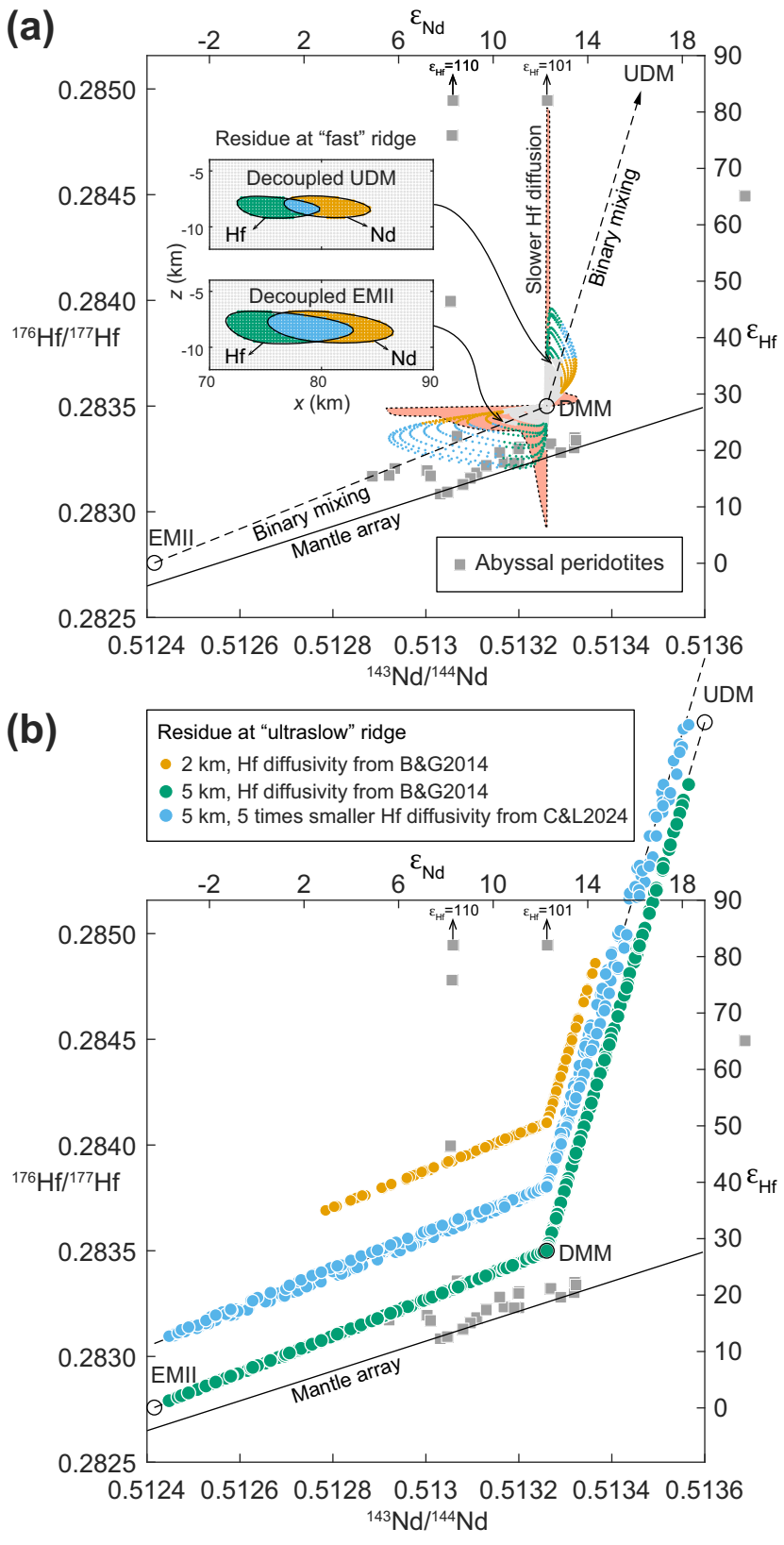

(caption on next page)

Fig. 8. Nd-Hf isotopic composition of residues beneath the "fast" ridge model (a) and "ultraslow" ridge model (b). The isotopic composition of EMII is the same as the case shown in Fig. 2. The isotope ratios of UDM are arbitrarily chosen to have $^{143}Nd/^{144}Nd = 0.5137$ and $^{176}Hf/^{177}Hf = 0.2845$. The abundance of Nd (or Hf) in EMII and UDM is assumed to be 1.5 and 0.5 times that of DMM. The diameter of original heterogeneity is 5 km in (a). Results of different original sizes are shown by more examples in Fig. S7 in supplementary material. The shape for Nd and Hf signals in the residue at the "fast" ridge model is illustrated in the insets inside panel (a). If the diffusivity of Hf is five times smaller (Cherniak and Liang, 2024, manuscript in preparation), the "fast" ridge model produces a vertical trend and a horizontal trend as a result of almost complete decoupling of Nd and Hf isotopic signals. Resulted shapes of Nd and Hf isotopic signals using smaller diffusivity of Hf are provided in Fig. S8 in supplementary material. Using the same endmember compositions, Nd-Hf isotopic compositions of the residue beneath the "ultraslow" ridge model fall on the binary mixing lines between endmembers in the source (b). The diameter of original heterogeneity is 5 km or 2 km. To visually separate results from different simulations, data points for Nd-Hf isotopic compositions for different diameters and Hf diffusivities are vertically elevated by different amounts. Data for abyssal peridotites are from literature (Stracke et al., 2011; Mallick et al., 2014, 2015; Sani et al., 2023). The mantle array is chosen from Chauvel et al. (2008).

(Chauvel et al., 2008). Although the "ultraslow" ridge model produces coupled Nd-Hf isotope ratios, decoupling cannot be ruled out for ultraslow-spreading ridges if the melt fraction is larger than currently estimated or the melt flux is stronger than that of the current model.

4.4. Uncertainties in model parameters

A crucial parameter determining the decoupling between Hf and Nd isotopic signals in the residue is the diffusivity of Hf in pyroxene. A recent study by Cherniak and Liang (2024) suggests that diffusivities of Hf in diopside and enstatite are 3–5 times slower than diffusivities of Hf in diopside reported in Bloch and Ganguly (2014). Simulations with five times smaller Hf diffusivity show that the transport velocity of Hf isotopic signal is slower (Fig. S9 in supplementary material). The slower diffusion of Hf increases the effective partition coefficient of Hf, making Hf even more compatible compared to Nd. Consequently, the Hf isotopic signal is further separated from the Nd isotopic signal. To better understand the effect of smaller diffusivity, we analyzed a simpler problem in 1D with constant velocities and uniform melt distribution (supplementary material). We show that the transport velocity of Hf for all wavelengths is reduced by 15% using slower diffusivity of Hf (Fig. S10 in supplementary material). The composition of residues produced using the "fast" ridge model demonstrates strong decoupling in Nd-Hf diagram (Fig. 8a). The observed trends exhibit two distinct components: a vertical trend and a horizontal trend. The vertical trend signifies a lag in the Hf signal compared to that of Nd. Conversely, the horizontal trend indicates a forward displacement of the Nd signal with respect to Hf. If the original size is smaller than 5 km, there would still exist two orthogonal trends but of shorter length due to stronger decay of Nd and Hf isotopic signals. However, if the size of the original heterogeneity were much larger than the observed physical displacement between Nd and Hf signals, which is 15 km (Fig. S8 in supplementary material), most compositions of the residue would stay coupled and fall on the binary mixing lines.

The extremely depleted Hf isotope ratios observed at Gakkel ridge above the mantle array are not likely to be caused by such strong decoupling in the most recent ridge process for two reasons. (1) The effective partition coefficient of Hf would be increased to 0.127 (Liang and Liu, 2016) which is much higher than the apparent partition coefficient of 0.035 for abyssal peridotites (Workman and Hart, 2005). (2) The decoupling requires a larger melt fraction not seen beneath Gakkel ridge. However, it is possible that previous melting events with large melt fraction (~1%, similar to present-day fast-spreading ridge) produced strongly decoupled Nd-Hf isotope ratios and the part with subvertical Nd-Hf trend gets recycled into some of the ultraslow ridges at present day.

The separation velocity at a given melt fraction depends strongly on the grain size and the choice of permeability model. Current simulation has utilized the permeability model of Wark and Watson (1998) that is among the lowest in the literature (von Bargen and Waff, 1986; Miller et al., 2014). Increasing the permeability by an order of magnitude would enlarge the maximum difference in effective velocities of Nd and Hf from 5% to 33% for "fast" ridge model (Table. S2 in supplementary material). For "ultraslow" ridge model, the difference in effective velocities would increase from 0.3% to 3%. Hence, we interpret the above results as representing the minimum extent of dispersion and displacement experienced by Nd and Hf signals.

4.5. Further discussion of the ridge model

The 2D ridge model presented in this study only captures the essential processes of melting and melt migration beneath mid-ocean ridges. An important simplification of our 2D ridge model is constant melting rate for all components in the source. The heterogeneous melting rate has both chemical and dynamic effects. For the chemical effect, if the enriched heterogeneity had a larger melting rate compared to the surrounding depleted mantle, its abundance of Nd would be more depleted relative to that in the surrounding mantle. Consequently, the enriched Nd isotope ratio in the heterogeneity may be reset by percolating melt with depleted isotope ratio. The higher melt productivity of the enriched heterogeneity would also increase the local melt flux, enhance dispersion, and promote mixing of melt and solid of different isotope ratios. On the other hand, if the ultra-depleted heterogeneity had smaller melting rate, the abundance of Nd in the heterogeneity would be higher than the case of uniform melting rate. The ultra-depleted heterogeneity would have smaller porosity and permeability, which hinders percolation of enriched melt through the ultra-depleted heterogeneity. Therefore, the chemical effect of heterogenous melting rate is to damp and preserve the isotope ratio of enriched and ultra-depleted heterogeneity, respectively.

Heterogeneous melting rate due to a spatially heterogeneous mantle also produce unsteady-state melt flow characterized by nonlinear porosity waves. Solitary waves and compaction-dissolution waves may arise in the melting region where large contrast in permeability exists (Scott and Stevenson, 1984; Barcilon and Richter, 1986; Spiegelman, 1993; Hesse et al., 2011). The melt flow field is highly time-dependent and local melt fraction can be considerably higher than that in the background (Richter and Daly, 1989; Watson and Spiegelman, 1994; Liang et al., 2011; Jordan et al., 2018). Existing results suggest that the signal with peak concentration and porosity splits into one carrying the original concentration traveling at a slow velocity and another faster-traveling porosity wave carrying concentration the same as the background (Richter and Daly, 1989). However, these simulations which assume local chemical equilibrium present a significant computational challenge. The incorporation of chemical disequilibrium could further complicate the preservation of chemical heterogeneities in the melting region, warranting further study.

Finally, realistic ridge segments exhibit a wider range of features, including oblique spreading, asymmetry about the axis, transform faults, etc. Oblique spreading at ultraslow ridges reduces the effective spreading rate which may suppress decompression melting (Montési and Behn, 2007). Transform faults have a cooling effect (Morgan and Forsyth, 1988). Current models predict negligible dispersion for ultraslow and slow-spreading ridges. These results remain valid under scenarios with potentially lower melt fractions arising from factors like oblique spreading or transform fault thermal effects. Asymmetric melt distribution has been found at EPR (Key et al., 2013). Mantle flow may be asymmetric and produce different shapes of chemical heterogeneities in the two sides across the central axis. Since the strength of dispersion increases with larger melt fraction, chemical heterogeneities in the side

with larger melt fraction are expected to experience stronger dispersion and mixing of isotope ratios. Residue rocks sampled at two sides across such ridge segment have the same source thus could be ideal tests for the effect of melt distribution. These features should be investigated in a case-by-case scenario.

5. Conclusions

This study predicts the patterns of deformation and dispersion of chemical heterogeneities marked by Nd-Hf isotope ratios in the residue at mid-ocean ridges. To examine the effect of melting and melt migration processes on the composition and shape of Nd-Hf isotopic heterogeneities, we set up two endmember ridge models that may correspond to fast and ultraslow-spreading ridges. We found that, to the first order, the melt fraction beneath a ridge controls the deformation pattern, the magnitude of dispersion, and the extent of Nd-Hf decoupling. Key findings are summarized as follows.

(1) The percolation of interstitial melt causes upward dispersion of chemical heterogeneity. The shape of chemical heterogeneity is dispersed in between the signal traveling at the velocity of the mantle and that of the percolating melt. Following a circle-shaped heterogeneity below the axis of a "fast" ridge model with maximum melt fraction of 1%, the shape is first stretched vertically. Above the depth of maximum melt fraction, reduced melt fraction in the residue slows down the effective transport velocity of incompatible trace elements and causes the vertically stretched heterogeneity to contract. For chemical heterogeneities following a corner flow trajectory, a subvertical dispersion tail is superimposed on the shear-induced oblate shape which then experiences additional shear below the lithosphere.
(2) The strength of dispersion strongly depends on melt fraction. If there was no melt beneath some amagmatic ridge segment at ultraslow-spreading centers, no dispersion would occur. In our "ultraslow" ridge model with maximum melt fraction of 0.2%, heterogeneities larger than 2 km in diameter experience negligible dispersion. The deformation of the chemical heterogeneity is controlled by the flow of the mantle. A circle-shaped chemical heterogeneity ends up as an oblate ellipse. The long axis of the deformed shape could reach two times the original diameter. This case is equivalent to perfect fractional melting.
(3) The decoupling of Nd-Hf isotopic signals in physical space depends on the difference in the effective transport velocities of Nd and Hf, which in turn are strongly controlled by the melt fraction, partition coefficient, and diffusivity. Beneath the "fast" ridge model, the effective vertical transport velocity of Nd could be 5% faster than Hf, which causes considerate chromatography fractionation of Nd and Hf signals. In "ultraslow" ridge model, the percolation of melt relative to the solid is slow and the effective transport velocities of Nd and Hf are close (within 0.3%). Consequently, Nd and Hf isotope ratios in the residue are coupled in Nd-Hf diagram and inherit the exact isotope ratios of the source mantle.
(4) Existing data suggests that diffusion of Hf in pyroxene is 2.5∼13 times slower than Nd. A previous melting event at an ancient fast-spreading ridge with ∼1% melt fraction could produce the residual peridotite with extremely depleted Hf isotope ratio that eventually gets recycled into the asthenosphere beneath a present day ultraslow-spreading ridge.
(5) The permeability model used in the current study may underestimate the separation rate of melt with respect to the solid. If the permeability is larger than the preferred estimate, Nd and Hf isotopic signals could be separated beneath slow and ultraslow-spreading ridges. The possibility of producing extremely decoupled Nd-Hf by recent melting processes beneath ultraslow-spreading ridges cannot be ruled out.

The variation of Nd-Hf isotope ratios in residue samples reflect both the source and processes. The current study emphasizes the role of mid-ocean ridge processes in the mixing and decoupling of Nd-Hf isotope ratios in residues sampled at different ridges. Global circulation of kilometer-scale chemical heterogeneities of both enriched and ultra-depleted compositions has produced the heterogeneous mantle source beneath individual ridges. Since mid-ocean ridges are globally distributed and have been active for billions of years, heterogeneities in the mantle are inevitably subjected to ridge processes, possibly multiple times over. It is necessary to evaluate melting processes before observations on residual rocks can be used to investigate the mantle beneath mid-ocean ridges.

One sentence summary

Two-dimensional flows of the solid and melt beneath mid-ocean ridges cause shearing, stretching, compression, and subvertical dispersion of pre-existing Nd-Hf isotopic heterogeneities in the mantle, leading to decoupled Nd-Hf isotope ratios in the residue.

CRediT authorship contribution statement

Boda Liu: Writing – review & editing, Writing – original draft, Visualization, Validation, Supervision, Software, Resources, Project administration, Methodology, Investigation, Funding acquisition, Formal analysis, Data curation, Conceptualization. **Yan Liang:** Writing – review & editing, Visualization, Validation, Supervision, Resources, Project administration, Methodology, Investigation, Funding acquisition, Formal analysis, Conceptualization. **Chuan-Zhou Liu:** Writing – review & editing, Validation, Supervision, Resources, Project administration, Investigation, Funding acquisition, Formal analysis.

Declaration of competing interest

The authors declare that they have no known competing financial interests or personal relationships that could have appeared to influence the work reported in this paper.

Data availability

The input file and code are available via a public data repository (Mendeley Data, V1, doi:10.17632/ttt9txmspd.1).

Acknowledgments

We thank Andreas Stracke and Bill White for constructive reviews. This study is funded by the Strategic Priority Program (Category B) of Chinese Academy of Sciences(no. XDB0710000). Work at Brown University by B. L and Y. L. was supported by US National Science Foundation grants OCE-1852088 and EAR-2147598. C.-Z. L acknowledges funding from Key Research Program of the Institute of Geology and Geophysics, CAS (IGGCAS-202202).

Supplementary materials

Supplementary material associated with this article can be found, in the online version, at doi:10.1016/j.epsl.2024.118925.

References

Baltzell, C., Parmentier, E.M., Liang, Y., Tirupathi, S., 2015. A high-order numerical study of reactive dissolution in an upwelling heterogeneous mantle: 2. Effect of shear deformation. Geochem. Geophys. Geosyst. 16, 3855–3869.
Barcilon, V., Richter, F.M., 1986. Nonlinear waves in compacting media. J. Fluid. Mech. 164, 429–448.

Bell, S., Ruan, Y., Forsyth, D.W., 2016. Ridge asymmetry and deep aqueous alteration at the trench observed from Rayleigh wave tomography of the Juan de Fuca plate. J. Geophys. Res.: Solid Earth 121, 7298–7321.
Bizimis, M., Sen, G., Salters, V.J.M., 2004. Hf–Nd isotope decoupling in the oceanic lithosphere: constraints from spinel peridotites from Oahu, Hawaii. Earth Planet. Sci. Lett. 217, 43–58.
Bloch, E., Ganguly, J., 2014. 176Lu–176Hf and 147Sm–143Nd ages of the Martian shergottites: evaluation of the shock-resetting hypothesis through diffusion kinetic experiments and modeling, and petrological observations. Earth Planet. Sci. Lett. 395, 173–183.
Bodinier, J.L., Vasseur, G., Vernieres, J., Dupuy, C., Fabries, J., 1990. Mechanisms of Mantle Metasomatism: geochemical Evidence from the Lherz Orogenic Peridotite. J. Petrol. 31, 597–628. https://doi.org/10.1093/petrology/31.3.597.
Bo, T., Katz, R.F., Shorttle, O., Rudge, J.F., 2018. The Melting Column as a Filter of Mantle Trace-Element Heterogeneity. Geochem. Geophys. Geosyst. 19, 4694–4721.
Braun, M.G., Hirth, G., Parmentier, E.M., 2000. The effects of deep damp melting on mantle flow and melt generation beneath mid-ocean ridges. Earth Planet. Sci. Lett. 176, 339–356.
Braun, M.G., Kelemen, P.B., 2002. Dunite distribution in the Oman Ophiolite: implications for melt flux through porous dunite conduits. Geochem. Geophys. Geosyst. 3, 1–21.
Chauvel, C., Lewin, E., Carpentier, M., Arndt, N.T., Marini, J.-C., 2008. Role of recycled oceanic basalt and sediment in generating the Hf-Nd mantle array. Nat. Geosci. 1, 64–67.
Cherniak, D., Liang, Y., 2024. Diffusion of Zr and Hf in clinopyroxene and orthopyroxene. In: Goldschmidt Conference abstract 24177.
Cipriani, A., Brueckner, H.K., Bonatti, E., Brunelli, D., 2004. Oceanic crust generated by elusive parents: Sr and Nd isotopes in basalt-peridotite pairs from the Mid-Atlantic Ridge. Geology 32, 657–660.
DePaolo, D.J., 1996. High-frequency isotopic variations in the Mauna Kea tholeiitic basalt sequence: melt zone dispersivity and chromatography. J. Geophys. Res.: Solid Earth 101, 11855–11864.
Forsyth, D.W., 1993. Crustal thickness and the average depth and degree of melting in fractional melting models of passive flow beneath mid-ocean ridges. J. Geophys. Res.: Solid Earth 98, 16073–16079.
Frisby, C., Bizimis, M., Mallick, S., 2016. Hf–Nd isotope decoupling in bulk abyssal peridotites due to serpentinization. Chem. Geol. 440, 60–72.
Gao, H., 2016. Seismic velocity structure of the Juan de Fuca and Gorda plates revealed by a joint inversion of ambient noise and regional earthquakes. Geophys. Res. Lett. 43, 5194–5201.
Harmon, N., Forsyth, D.W., Weeraratne, D.S., 2009. Thickening of young Pacific lithosphere from high-resolution Rayleigh wave tomography: a test of the conductive cooling model. Earth Planet. Sci. Lett. 278, 96–106.
Hebert, L.B., Montési, L.G.J., 2010. Generation of permeability barriers during melt extraction at mid-ocean ridges. Geochem. Geophys. Geosyst. 11.
Hesse, M.A., Schiemenz, A.R., Liang, Y., Parmentier, E.M., 2011. Compaction–dissolution waves in an upwelling mantle column. Geophys. J. Int. 187, 1057–1075.
Holtzman, B.K., Kohlstedt, D.L., Zimmerman, M.E., Heidelbach, F., Hiraga, T., Hustoft, J., 2003. Melt Segregation and Strain Partitioning: implications for Seismic Anisotropy and Mantle Flow. Science 301, 1227–1230.
Iwamori, H., 1993a. Dynamic disequilibrium melting model with porous flow and diffusion-controlled chemical equilibration. Earth Planet. Sci. Lett. 114, 301–313.
Iwamori, H., 1993b. A model for disequilibrium mantle melting incorporating melt transport by porous and channel flows. Nature 366, 734–737.
Jackson, M.G., Hart, S.R., 2006. Strontium isotopes in melt inclusions from Samoan basalts: implications for heterogeneity in the Samoan plume. Earth Planet. Sci. Lett. 245, 260–277.
Johnson, K.T.M., Dick, H.J.B., 1992. Open system melting and temporal and spatial variation of peridotite and basalt at the Atlantis II Fracture Zone. J. Geophys. Res.: Solid Earth 97, 9219–9241.
Johnson, K.T.M., Dick, H.J.B., Shimizu, N., 1990. Melting in the oceanic upper mantle: an ion microprobe study of diopsides in abyssal peridotites. J. Geophys. Res.: Solid Earth 95, 2661–2678.
Jordan, J.S., Hesse, M.A., Rudge, J.F., 2018. On mass transport in porosity waves. Earth Planet. Sci. Lett. 485, 65–78.
Jull, M., Kelemen, P.B., Sims, K., 2002. Consequences of diffuse and channelled porous melt migration on uranium series disequilibria. Geochim. Cosmochim. Acta 66, 4133–4148.
Katz, R.F., Weatherley, S.M., 2012. Consequences of mantle heterogeneity for melt extraction at mid-ocean ridges. Earth Planet. Sci. Lett. 335–336, 226–237.
Kelemen, P.B., Hirth, G., Shimizu, N., Spiegelman, M., Dick, H.J.B., 1997. A review of melt migration processes in the adiabatically upwelling mantle beneath oceanic spreading ridges. Philosoph. Transact.: Math., Phys. Eng. Sci. 355, 283–318.
Key, K., Constable, S., Liu, L., Pommier, A., 2013. Electrical image of passive mantle upwelling beneath the northern East Pacific Rise. Nature 495, 499–502.
Langmuir, C.H., Bender, J.F., Bence, A.E., Hanson, G.N., Taylor, S.R., 1977. Petrogenesis of basalts from the FAMOUS area: Mid-Atlantic Ridge. Earth Planet. Sci. Lett. 36, 133–156.
Langmuir, C.H., Vocke Jr., R.D., Hanson, G.N., Hart, S.R., 1978. A general mixing equation with applications to Icelandic basalts. Earth and Planetary Science Letters 37, 380–392.
Liang, Y., 2003. On the thermo-kinetic consequences of slab melting. Geophys. Res. Lett. 30, 2270.
Liang, Y., 2008. Simple models for dynamic melting in an upwelling heterogeneous mantle column: analytical solutions. Geochim. Cosmochim. Acta 72, 3804–3821.
Liang, Y., 2020. Trace element fractionation and isotope ratio variation during melting of a spatially distributed and lithologically heterogeneous mantle. Earth Planet. Sci. Lett. 552, 116594.
Liang, Y., Liu, B., 2016. Simple models for disequilibrium fractional melting and batch melting with application to REE fractionation in abyssal peridotites. Geochim. Cosmochim. Acta 173, 181–197.
Liang, Y., Liu, B., 2018. Stretching chemical heterogeneities by melt migration in an upwelling mantle: an analysis based on time-dependent batch and fractional melting models. Earth Planet. Sci. Lett. 498, 275–287.
Liang, Y., Peng, Q., 2010. Non-modal melting in an upwelling mantle column: Steady-state models with applications to REE depletion in abyssal peridotites and the dynamics of melt migration in the mantle. Geochim. Et Cosm. Acta. 74, 321–339. https://doi.org/10.1016/j.gca.2009.09.029.
Liang, Y., Schiemenz, A., Hesse, M.A., Parmentier, E.M., 2011. Waves, channels, and the preservation of chemical heterogeneities during melt migration in the mantle. Geophys. Res. Lett. 38.
Liu, B., Liang, Y., 2017a. The prevalence of kilometer-scale heterogeneity in the source region of MORB upper mantle. Sci. Adv. 3.
Liu, B., Liang, Y., 2017b. An introduction of Markov chain Monte Carlo method to geochemical inverse problems: reading melting parameters from REE abundances in abyssal peridotites. Geochim. Cosmochim. Acta 203, 216–234.
Liu, B., Liang, Y., 2019. Importance of permeability and deep channel network on the distribution of melt, fractionation of REE in abyssal peridotites, and U-series disequilibria in basalts beneath mid-ocean ridges: a numerical study using a 2D double-porosity model. Earth Planet. Sci. Lett. 528, 115788.
Liu, B., Liang, Y., 2020. Importance of the size and distribution of chemical heterogeneities in the mantle source to the variations of isotope ratios and trace element abundances in mid-ocean ridge basalts. Geochim. Cosmochim. Acta 268, 383–404.
Lundstrom, C., 2000. Models of U-series disequilibria generation in MORB: the effects of two scales of melt porosity. Phys. Earth Planet. Inter. 121, 189–204.
Mallick, S., Dick, H.J.B., Sachi-Kocher, A., Salters, V.J.M., 2014. Isotope and trace element insights into heterogeneity of subridge mantle. Geochem. Geophys. Geosyst. 15, 2438–2453.
Mallick, S., Standish, J.J., Bizimis, M., 2015. Constraints on the mantle mineralogy of an ultra-slow ridge: Hafnium isotopes in abyssal peridotites and basalts from the 9–25°E Southwest Indian Ridge. Earth Planet. Sci. Lett. 410, 42–53.
McCulloch, M.T., Gregory, R.T., Wasserburg, G.J., Taylor Jr., H.P., 1981. Sm-Nd, Rb-Sr, and $^{18}O/^{16}O$ isotopic systematics in an oceanic crustal section: evidence from the Samail Ophiolite. J. Geophys. Res.: Solid Earth 86, 2721–2735.
McKenzie, D., 1984. The generation and compaction of partially molten rock. J. Petrol. 25, 713–765.
Miller, K.J., Zhu, W.-l., Montési, L.G.J., Gaetani, G.A., 2014. Experimental quantification of permeability of partially molten mantle rock. Earth Planet. Sci. Lett. 388, 273–282.
Montési, L.G.J., Behn, M.D., 2007. Mantle flow and melting underneath oblique and ultraslow mid-ocean ridges. Geophys. Res. Lett. 34.
Morgan, J.P., Forsyth, D.W., 1988. Three-dimensional flow and temperature perturbations due to a transform offset: effects on oceanic crustal and upper mantle structure. J. Geophys. Res.: Solid Earth 93, 2955–2966.
Morgan, J.P., 1987. Melt migration beneath mid-ocean spreading centers. Geophys. Res. Lett. 14, 1238–1241.
Navon, O., Stolper, E., 1987. Geochemical consequences of melt percolation: the upper mantle as a chromatographic column. J. Geol. 95, 285–307.
Niu, Y., Langmuir, C.H., Kinzler, R.J., 1997. The origin of abyssal peridotites: a new perspective. Earth Planet. Sci. Lett. 152, 251–265.
Niu, Y., Hékinian, R., 1997. Spreading-rate dependence of the extent of mantle melting beneath ocean ridges. Nature 385, 326–329.
Parmentier, E.M., Morgan, J.P., 1990. Spreading rate dependence of three-dimensional structure in oceanic spreading centres. Nature 348, 325–328.
Qin, Z., 1992. Disequilibrium partial melting model and its implications for trace element fractionations during mantle melting. Earth Planet. Sci. Lett. 112, 75–90.
Richter, F.M., 1986. Simple models for trace element fractionation during melt segregation. Earth Planet. Sci. Lett. 77, 333–344.
Richter, F.M., Daly, S.F., 1989. Dynamical and chemical effects of melting a heterogeneous source. J. Geophys. Res.: Solid Earth 94, 12499–12510.
Rioux, M., Bowring, S., Kelemen, P., Gordon, S., Dudás, F., Miller, R., 2012. Rapid Crustal Accretion and Magma Assimilation in the Oman-U.A.E. Ophiolite: High Precision U-Pb Zircon Geochronology of the Gabbroic Crust, 117.
Sanfilippo, A., Salters, V., Tribuzio, R., Zanetti, A., 2019. Role of ancient, ultra-depleted mantle in Mid-Ocean-Ridge magmatism. Earth Planet. Sci. Lett. 511, 89–98.
Saikia, U., Rychert, C., Harmon, N., Kendall, J.M., 2021. Upper Mantle Anisotropic Shear Velocity Structure at the Equatorial Mid-Atlantic Ridge Constrained by Rayleigh Wave Group Velocity Analysis From the PI-LAB Experiment, 22, e2020GC009495.
Salters, V.J.M., Hart, S.R., 1991. The mantle sources of ocean ridges, islands and arcs: the Hf-isotope connection. Earth Planet. Sci. Lett. 104, 364–380.
Salters, V.J.M., Zindler, A., 1995. Extreme $^{176}Hf/^{177}Hf$ in the sub-oceanic mantle. Earth Planet. Sci. Lett. 129, 13–30.
Salters, V.J.M., Dick, H.J.B., 2002. Mineralogy of the mid-ocean-ridge basalt source from neodymium isotopic composition of abyssal peridotites. Nature 418, 68–72.
Sani, C., Sanfilippo, A., Peyve, A.A., Genske, F., Stracke, A., 2023. Earth Mantle's Isotopic Record of Progressive Chemical Depletion, 4, e2022AV000792.
Scott, D.R., Stevenson, D.J., 1984. Magma solitons. Geophys. Res. Lett. 11, 1161–1164.
Snow, J.E., Hart, S.R., Dick, H.J.B., 1994. Nd and Sr isotope evidence linking mid-ocean-ridge basalts and abyssal peridotites. Nature 371, 57–60.

Sparks, D.W., Parmentier, E.M., 1991. Melt extraction from the mantle beneath spreading centers. Earth Planet. Sci. Lett. 105, 368–377.
Spiegelman, M., 1993. Physics of melt extraction: theory, implications and applications. Philosoph. Transact.: Phys. Sci. Eng. 342, 23–41.
Spiegelman, M., McKenzie, D., 1987. Simple 2-D models for melt extraction at mid-ocean ridges and island arcs. Earth Planet. Sci. Lett. 83, 137–152.
Stracke, A., Bizimis, M., Salters, V.J.M., 2003. Recycling oceanic crust: quantitative constraints. Geochem. Geophys. Geosyst. 4 n/a-n/a.
Stracke, A., Snow, J.E., Hellebrand, E., von der Handt, A., Bourdon, B., Birbaum, K., Günther, D., 2011. Abyssal peridotite Hf isotopes identify extreme mantle depletion. Earth Planet. Sci. Lett. 308, 359–368.
Sun, C., Liang, Y., 2012. Distribution of REE between clinopyroxene and basaltic melt along a mantle adiabat: effects of major element composition, water, and temperature. Contribut. Mineral. Petrol. 163, 807–823.
Sun, C., Liang, Y., 2014. An assessment of subsolidus re-equilibration on REE distribution among mantle minerals olivine, orthopyroxene, clinopyroxene, and garnet in peridotites. Chem. Geol. 372, 80–91.
The MELT Seismic Team, 1998. Imaging the deep seismic structure beneath a Mid-Ocean Ridge: the MELT experiment. Science 280, 1215–1218.
Tilhac, R., Begg, G.C., O'Reilly, S.Y., Griffin, W.L., 2022. A global review of Hf-Nd isotopes: new perspectives on the chicken-and-egg problem of ancient mantle signatures. Chem. Geol. 609, 121039.
Van Orman, J.A., Grove, T.L., Shimizu, N., 2002. Diffusive fractionation of trace elements during production and transport of melt in Earth's upper mantle. Earth Planet. Sci. Lett. 198, 93–112.
von Bargen, N., Waff, H.S., 1986. Permeabilities, interfacial areas and curvatures of partially molten systems: results of numerical computations of equilibrium microstructures. J. Geophys. Res.: Solid Earth 91, 9261–9276.
Wendt, J.I., Regelous, M., Niu, Y., Hékinian, R., Collerson, K.D., 1999. Geochemistry of lavas from the Garrett Transform Fault: insights into mantle heterogeneity beneath the eastern Pacific. Earth Planet. Sci. Lett. 173, 271–284. https://doi.org/10.1016/S0012-821X(99)00236-8.
Wang, S., Constable, S., Rychert, C.A., Harmon, N., 2020. A lithosphere-asthenosphere boundary and partial melt estimated using marine magnetotelluric data at the Central Middle Atlantic Ridge. Geochem. Geophys. Geosyst. 21, e2020GC009177.
Wark, D.A., Watson, E.B., 1998. Grain-scale permeabilities of texturally equilibrated, monomineralic rocks. Earth Planet. Sci. Lett. 164, 591–605. https://doi.org/10.1016/S0012-821X(98)00252-0.
Warren, J.M., 2016. Global variations in abyssal peridotite compositions. Lithos 248–251, 193–219.
Warren, J.M., Shimizu, N., 2010. Cryptic variations in abyssal peridotite compositions: evidence for shallow-level melt infiltration in the oceanic lithosphere. J. Petrol. 51, 395–423.
Warren, J.M., Shimizu, N., Sakaguchi, C., Dick, H.J.B., Nakamura, E., 2009. An assessment of upper mantle heterogeneity based on abyssal peridotite isotopic compositions. J. Geophys. Res.: Solid Earth 114, B12203.
Watson, S., Spiegelman, M., 1994. Geochemical effects of magmatic solitary waves—I. Numerical results. Geophys. J. Int. 117, 284–295.
Workman, R.K., Hart, S.R., 2005. Major and trace element composition of the depleted MORB mantle (DMM). Earth Planet. Sci. Lett. 231, 53–72.
Yao, L., Sun, C., Liang, Y., 2012. A parameterized model for REE distribution between low-Ca pyroxene and basaltic melts with applications to REE partitioning in low-Ca pyroxene along a mantle adiabat and during pyroxenite-derived melt and peridotite interaction. Contribut. Mineral. Petrol. 164, 261–280.
Yoshikawa, M., Python, M., Tamura, A., Arai, S., Takazawa, E., Shibata, T., Ueda, A., Sato, T., 2015. Melt extraction and metasomatism recorded in basal peridotites above the metamorphic sole of the northern Fizh massif, Oman ophiolite. Tectonophysics 650, 53–64.
Zindler, A., Hart, S., 1986. Chemical Geodynamics. Annu. Rev. Earth Planet. Sci. 14, 493–571.